Spatial and size-resolved electrostatic-directed deposition of nanoparticles on a field-generating substrate: theoretical and experimental analysis

D-H Tsai[1,2,3]**, T Hawa**[1,2,3]**, H-C Kan**[4,5]**, R J Phaneuf**[4,5] **and M R Zachariah**[1,2,3,6]

[1] Department of Mechanical Engineering, University of Maryland, College Park, USA

[2] Department of Chemistry and Biochemistry, University of Maryland, College Park, USA

[3] The National Institute of Standards and Technology, USA

[4] Laboratory for Physical Science, College Park, MD 20740, USA

[5] Department of Materials Science and Engineering, University of Maryland, College Park, MD 20740, USA

E-mail: mrz@umd.edu

Abstract

We build on our prior work on electrostatically directed nanoparticle assembly on a field-generating substrate (Tsai *et al* 2005 *Nanotechnology* **16** 1856–62). In this paper we develop a data set for particle size-resolved deposition, from which a Brownian dynamics model for the process can be evaluated. We have developed a trajectory model applied to positioning metal nanoparticles from the gas phase onto electrostatic patterns generated by biasing p–n junction substrates. Brownian motion and fluid convection of nanoparticles, as well as the interactions between the charged nanoparticles and the patterned substrate, including electrostatic force, image force and van der Waals force, are accounted for in the simulation. Using both experiment and simulation we have investigated the effects of the particle size, electric field intensity, and the convective flow on coverage selectivity. Coverage selectivity is most sensitive to electric field, which is controlled by the applied reverse bias voltage across the p–n junction. A non-dimensional analysis of the competition between the electrostatic and diffusion force is found to provide a means to collapse a wide range of process operating conditions and is an effective indicator of process performance.

(Some figures in this article are in colour only in the electronic version)

Nomenclature

T	System temperature (K)		U	Free stream velocity (m s^{-1})
k	Boltzmann constant (1.38×10^{-23} J K^{-1})		v_g	Convective flow velocity (m s^{-1})
$-V_{bias}$	Reverse bias voltage (V)		ε_s	Permittivity of medium
			Δt	Time step (s)
			n	Number of unit charges on a particle

[6] Author to whom any correspondence should be addressed.

m_p	Mass of a particle (kg)
d	Diameter of a particle (m)
S	Particle–particle shortest distance (m)
B	Particle mobility (N^{-1} m s^{-1})
β	Friction constant
C_c	Slip correction factor
D	Diffusivity of a particle (m^2 s^{-1})
μ	Viscosity of N_2 (1.77×10^{-5} N s m^{-2})
λ	Mean free path of the gas (m)
ρ_g	Density of N_2 (kg m^{-3})

1. Introduction

Functional nanoparticles have been widely considered as the building blocks of potential electronic, optoelectronic, and sensing devices [1, 2]. For many applications of nanoparticles, in for example sensors or other electronic devices, precise positioning for integration into a working device becomes a considerable challenge. The production of nanoparticles using gas-phase methods has the advantage of a clean, continuous process which can be operated at atmospheric conditions without requiring any vacuum environment or solvent medium [2]. An additional advantage is that charge can be readily placed on nanoparticles, which can be used both to conduct size selection or filtration, and to direct deposition through the implementation of electric fields. Electrostatic-directed methods have been used previously with some success [3–6], and they suggest a good strategy to achieve this alignment. In our previous work [6], we directed the deposition of particles using a substrate with lateral and vertical tunable fields. This was achieved by using an array of biased p–n junction-patterned substrates to generate a pattern of tunable electric fields, which enabled us to form stable charge patterns on the substrate. Using unipolarly charged Ni nanoparticles we observed that with sufficient reverse bias on the p–n junction we could achieve selective deposition on the specific positions on the substrate. Under the right conditions we achieved very high coverage selectivity (∼100%), and stripe-like deposition patterns of nanoparticles (∼500 nm in width).

The success of this work suggested further investigation into the particle size dependence of coverage selectivity, and some consideration of the ultimate resolution that could be achieved in this patterning approach. In this paper we discuss an expanded set of experiments using size-segregated (monodisperse) particles. These data form the basis for the development of a validated Brownian dynamics model.

2. Experimental details

To understand the nature of the deposition process we employ an approach to prepare unipolarly charged nanoparticles with a very narrow size distribution (∼ monodisperse). Figure 1(a) presents a schematic diagram of our experimental system. Silver nanoparticles were synthesized by a spray pyrolysis method [7]. The choice of silver was based on an eventual goal of using these particles for surface plasmon resonance (SPR) biosensing devices [8]. A silver nitrate (99+%, Aldrich)/water solution was atomized into droplets (∼2 μm) and passed to a 850 °C flow reactor in nitrogen. At this temperature the metal nitrate is converted to a pure silver aerosol with a rather

wide particle size distribution [21, 22]. We employ ion-mobility separation of charged particles to create a narrow size cut using a differential mobility analyzer (DMA) [6, 9, 23]. The output of the DMA, which operates like a band-pass filter, provides an output of unipolar charged monodisperse aerosol. The number concentration of monodisperse particles was ∼10^5–10^6 cm^{-3} at a flow rate of 1 lpm (litres per minute). These aerosol particles were then delivered to a second tube-furnace at 600–800 °C for the purpose of creating spherical nanoparticles. A unipolar charging process [6, 10] was applied to maximize the charges before deposition. These nanoparticles were delivered to the deposition chamber. A more detailed description of the nature of the p–n junction substrate can be found in our previous publication [6]. Briefly, the p–n junction-patterned substrate was n-type GaAs (Si doped, 10^{18} cm^{-3}) coated with SiO_2. Photolithography was used to define lines for the p-type doping. The p-type doping was created by ion implantation of Zn^+ ions (10^{19} cm^{-3}) through the SiO_2 layer. The photoresist was then removed and the oxide layer stripped before rapid thermal annealing for activation of the Zn^+ ions. Reverse bias was applied by connecting the p-type doped contact pad with the cathode of the DC power supply, and the n-type doped substrate with the anode of the power supply. For particle deposition, the p–n junction-patterned substrate was placed in a deposition chamber (9 cm internal diameter and 10 cm in height) with an aerosol feed nozzle (2 mm internal diameter) 1 cm above the substrate.

We prepared three different sized Ag nanoparticles, 30, 50, and 70 nm in diameter, for our studies. The deposition process was the same as we described in our previous work [6], and is schematically shown in figure 2. For this study, we chose to work with negatively charged particles. The applied reverse bias voltage across the substrate was varied from 0.1 to 0.9 V, and the current measured was always less than 0.02 mA. A two-dimensional (2D) electric field is generated from the depletion regions of the p–n junction and is employed to steer the incoming nanoparticles flowing in the boundary layer (details are described in section 3). The nanoparticle deposition pattern was observed with a Hitachi S-4000 field emission scanning electron microscope (SEM) operated at 4–6 kV.

To quantify the difference in particle deposition between the p-type and n-type regions, we define a coverage selectivity of n-type to p-type regions as follows [6].

$$\text{Coverage selectivity} = \frac{C_N - C_P}{C_N} \times 100\% \qquad (1)$$

where C_P and C_N are the coverage of particles deposited on the p-type and the n-type regions determined by digital processing of the SEM images.

3. Theoretical model of electrostatic-directed assembly

In this study we have developed a trajectory model based on the force balance on an individual particle approaching the surface of a p–n junction-patterned substrate. The flow field is illustrated in figure 1(b). For a stagnation point flow, such as we have, the flow carrying the nanoparticles will turn parallel to the substrate, to form the boundary layer [11, 12].
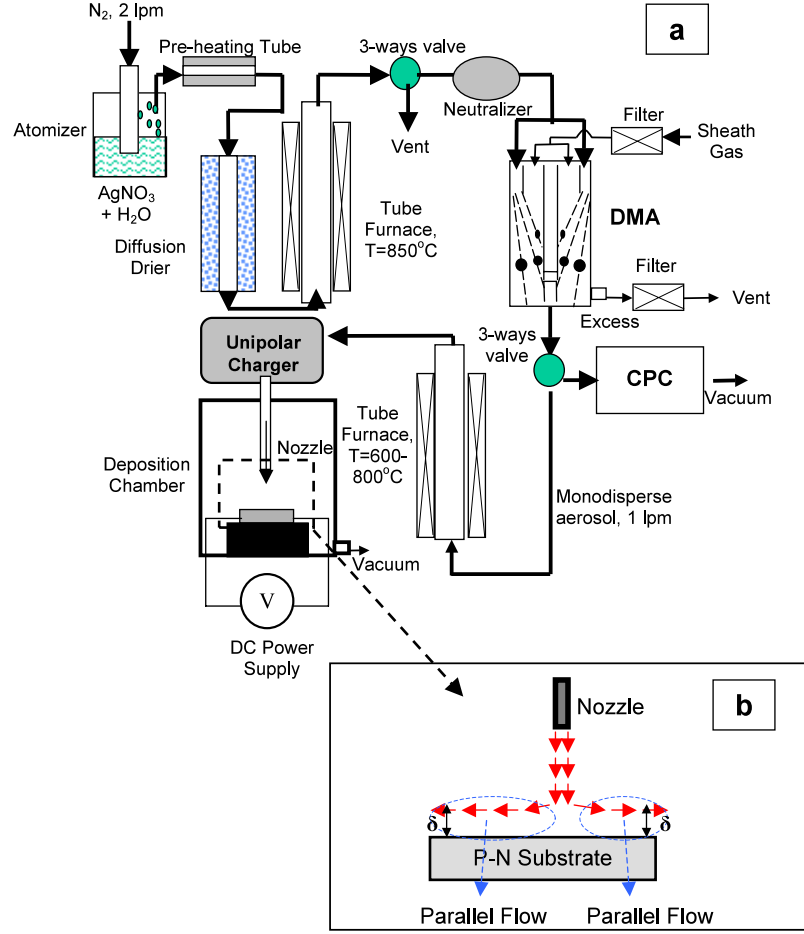
Figure 1. (a) Schematic of the experimental system. (DMA: differential mobility analyzer; CPC: condensation particle counter). (b) Flow field above a p–n junction-patterned surface. δ represents the thickness of boundary layer.

We analyze the nanoparticle patterns at a location 0.3 cm from the stagnant point ($x_f = 0.3$ cm), where the flow is essentially parallel to the substrate. From a mass balance the boundary layer integrated velocity parallel to the substrate can be evaluated.

$$Q = (\pi x_f) \times \delta \times U. \tag{2}$$

Here, Q is the flow rate of carrier gas ($\sim$1 lpm), and U is the free stream velocity. For a stagnation point flow the boundary layer thickness δ can be estimated as [11]

$$\delta = \frac{5x_f}{\sqrt{\frac{\rho_g U x_f}{\mu}}}. \tag{3}$$

Here, ρ_g is the density of N_2 carrier gas, and μ is its viscosity.

Using typical values yields $\delta \sim 1$ mm. For a stagnation flow the convective flow velocity parallel to the substrate can be expressed as a function of height Y_f above the substrate as [11]

$$v_g = U \sin\left(\frac{\pi Y_f}{2\delta}\right). \tag{4}$$

The deposition process of nanoparticles can be thought to involve two limiting regimes [12]. In regime 1 the weak interaction between the incoming particle and the substrate means that particle motion is governed by convective and Brownian motion. In regime 2 the particles are sufficiently close to the substrate, such that the interaction between an incoming nanoparticle and the substrate strongly influences the particle trajectory [6, 12]. The net external force acting on a particle, $\vec{F}_{ext}$, is given by

$$\vec{F}_{ext} = \vec{F}_e + \vec{F}_i + \vec{F}_{vdw}, \tag{5}$$

where $\vec{F}_i$ and $\vec{F}_{vdw}$ are the image and van der Waals, respectively, and where $\vec{F}_e$ is the electrostatic force between a charged particle and the charges generated from the depletion zones of the p–n junctions. It can be evaluated from n, the number of unit charges on a particle, and E, the electric field.

$$\vec{F}_e = ne\vec{E}. \tag{6}$$

For our experimental conditions, nearly all particles are singly charged as they exit the mobility classifier; therefore $n = 1$ [13, 14]. For the electric field, $\vec{E}$, we first solve the Laplacian equation $\nabla^2 V = 0$ [15] for the electrical potential distribution, $V(X, Y)$, near the substrate. Due to the linear nature of the substrate patterning, we solve the Laplacian equation in two dimensions, with the following boundary conditions.

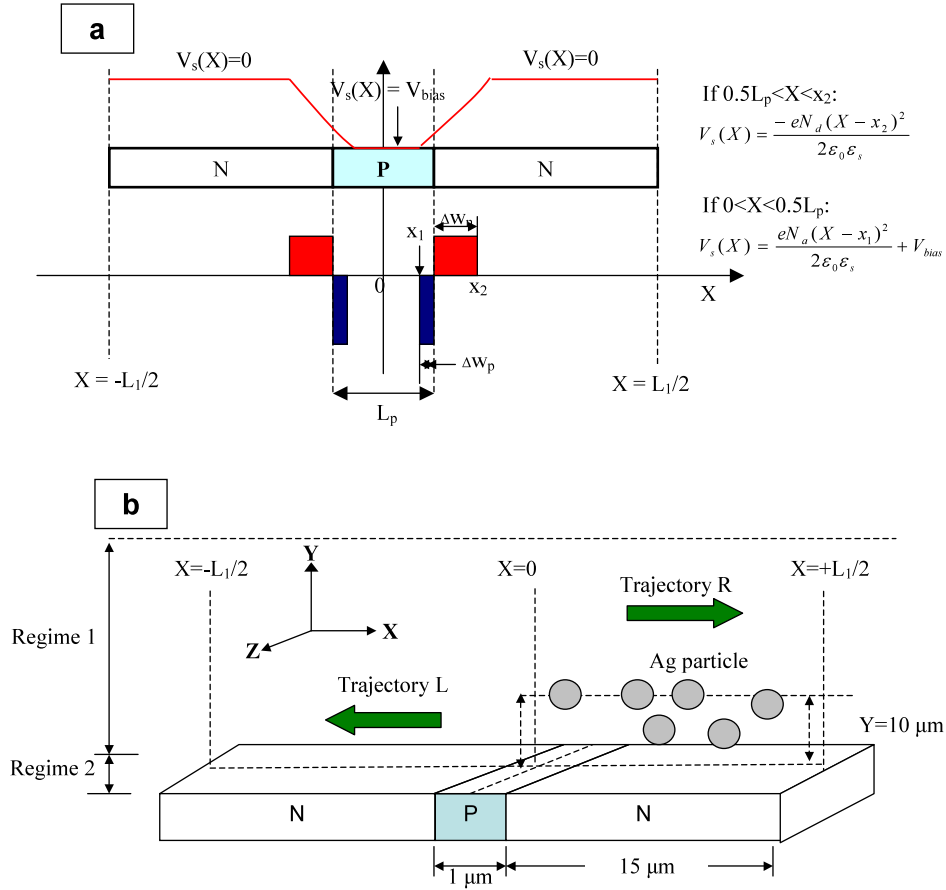$$V\left(-\frac{L_1}{2}, Y\right) = V\left(\frac{L_1}{2}, Y\right) \tag{7a}$$

Figure 2. (a) Description of the surface potential, V_s, of a reverse-biased p–n junction. (b) Description of our trajectory model. Two pairs of p–n junctions are located in the specific position of a control volume with a periodic boundaries between $X = -L_1/2$ and $X = +L_1/2$. The length of the n-type region is 30 μm, and the length of the p-type region is 1 μm. The initial position of particles for initialization of trajectories is $Y \leqslant 10$ μm, and $0 < X < L_1/2$. Regime 1 is at $Y > 200$ nm, and regime 2 is at $0.5d < Y < 200$ nm. d is the particle diameter.

$$\left.\frac{\partial V}{\partial X}\right|_{X=-\frac{L_1}{2}} = \left.\frac{\partial V}{\partial X}\right|_{X=\frac{L_1}{2}} \tag{7b}$$

$$V(X,0) = V_s(X) \tag{7c}$$

$$-\left.\frac{\partial V}{\partial Y}\right|_{Y=H} = E_H, \tag{7d}$$

where the X-coordinate is the direction parallel to the substrate surface and normal to the p-stripes, the Y-coordinate is normal to the substrate surface, and L_1 is the spatial period of the p–n junction array, i.e. the sum of the widths of the p-type and the width of the n-type regions. V_s (X) is the surface potential across the p–n junction, and E_H the electric field strength at the position H above the substrate. Equations (7a) and (7b) specify the periodic boundary conditions in the X-direction, equation (7c) specifies the potential on the p–n substrate, and equation (7d) specifies that the E-field beyond a vertical distance H from the substrate be uniform. We employ a simplified model for the potential $V_s(X)$ on the substrate surface, assuming the abrupt junction model and step-wise charge distributions for the depletion region. Based on these assumptions, the lateral variation of $V_s(X)$ can be written explicitly as shown in figure 2(a), where $x_2 = L_p/2 + \Delta w_n$ and $x_1 = L_p/2 - \Delta w_p$. $(-V_{bias})$ is the reverse bias voltage

applied across the p–n junction. N_a is the ionized acceptor concentration in the p-type region ($\sim 10^{19}$ cm^{-3}), and N_d is the ionized donor concentration in the n-type region ($\sim 10^{18}$ cm^{-3}), Δw_n and Δw_p are the widths of the depletion zone in n-type and p-type regions, respectively [6], e is the unit charge (1.6 $\times$ 10^{-19} C), ε_s, is the dielectric constant of GaAs (13.1), and ε_0 is the permittivity of free space. The analytical solution of the electrostatic potential distribution for the boundary conditions described above is the following.

$$V(X,Y) = K_1 + \frac{4e}{\varepsilon_0 \varepsilon_s L_1} \sum_{N=1} \left(N_a \sin(k_n x_1) + N_d \sin(k_n x_2) \right.$$
$$\left. - (N_a + N_d)\sin\left(\frac{k_n L_p}{2}\right)\right)\frac{\cos(k_n X)}{k_n^3}e^{-k_n Y} \tag{8}$$

$$K_1 = \frac{e(N_a \Delta w_p^3 + N_d \Delta w_n^3)}{3\varepsilon_0 \varepsilon_s L_1} + (-V_{bias})\left(1 - \frac{L_p}{L_1}\right), \tag{9}$$

where $k_n = 2N\pi/L_1$, and the corresponding electric field components E_x and E_y are

$$E_x = -\frac{dV}{dX}, \tag{10}$$

$$E_y = -\frac{dV}{dY}, \tag{11}$$

which are linear in $(-V_{\text{bias}})$. In addition to the applied electrical force, we also consider the image and van der Waals forces in equation (5) as given by [12]

$$F_{\text{i}} = -\frac{(ne)^2}{4\pi\varepsilon_{N_2}\varepsilon_0(2Y_{\text{f}})^2}\frac{\varepsilon_{\text{GaAs}} - \varepsilon_{N_2}}{\varepsilon_{\text{GaAs}} + \varepsilon_{N_2}} \tag{12}$$

$$F_{\text{vdw}} = -\frac{2A_H}{3}\frac{\left(\frac{d}{2}\right)^3}{\left(Y_{\text{f}} - \frac{d}{2}\right)^2\left(Y_{\text{f}} + \frac{d}{2}\right)^2}. \tag{13}$$

By combining the effects of the external forces, drag, convective flow, and Brownian motion, we can obtain analytic solutions for the particle trajectories by integrating the Langevin equation [16, 17]. The analytical solutions of the velocity and the displacement of a particle in the X-direction during a characteristic time step, $\Delta t = t_N - t_{N-1}$, are given by

$$v_{x,N} = v_{x,N-1}\text{e}^{-\beta\Delta t} + \frac{F_{x,N-1}}{m_{\text{p}}\beta}(1 - \text{e}^{-\beta\Delta t}) + B_{1,x} \tag{14}$$

$$x_N = x_{N-1} + \frac{1}{\beta}\left(v_{x,N} + v_{x,N-1} - \frac{2F_{x,N-1}}{m_{\text{p}}\beta}\right)$$
$$\times \left(\frac{1 - \text{e}^{-\beta\Delta t}}{1 + \text{e}^{-\beta\Delta t}}\right) + \frac{F_{x,N-1}}{m_{\text{p}}\beta}\Delta t + v_{\text{g}}\Delta t + B_{2,x}. \tag{15}$$

We can use similar forms to describe the motion in the Y- and Z-directions except that v_{g} is assumed to be zero in both the Y- and Z-directions, and F_{i} and F_{vdw}, which depend only depend on the vertical separation distance, are added to the component of the force acting in the Y-direction. In equations (14) and (15) B_1 and B_2 are random functions of time used to express Brownian motion of a particle, both of which follow a Gaussian distribution, with a mean value of zero. The mean-square values of B_1 and B_2 are expressed in the following:

$$\langle B_{1,x}^2 \rangle = \frac{kT}{m_{\text{p}}}(1 - \text{e}^{-2\beta\Delta t}) \tag{16}$$

$$\langle B_{2,x}^2 \rangle = \frac{2kT}{m_{\text{p}}\beta^2}\left[\beta\Delta t - 2\left(\frac{1 - \text{e}^{-\beta\Delta t}}{1 + \text{e}^{-\beta\Delta t}}\right)\right]. \tag{17}$$

Here, k is the Boltzmann constant, T is the temperature, m_{p} is the mass of a particle, β is the friction constant ($\beta = \frac{3\pi\mu d}{m_{\text{p}}C_{\text{c}}}$), and β^{-1} represents t_{r}, the relaxation time of a particle. N is the step number, C_{c} is the slip correction factor of a particle ($C_{\text{c}} = 1 + \frac{\lambda}{d}[2.34 + 1.05\exp(-0.39\frac{d}{\lambda})]$) [18], λ is the gas mean free path, and d is the particle diameter. For the size range we consider, $C_{\text{c}} \propto {\sim}d^{-1}$.

To describe the effects of diffusion, the diffusion force is also calculated from [19].

$$F_{\text{diff}} = \left(\frac{6\pi\mu dkT}{C_{\text{c}}\Delta t}\right)^{0.5}. \tag{18}$$

4. Simulation methodology

In our model, we focus on the incoming particle–substrate interaction, and the resulting coverage selectivity of nanoparticles deposited on the patterned substrate. Figure 2(b) is a schematic diagram of our trajectory model in a control volume. In the X-coordinate, a pair of p–n junctions bound the

Table 1. Simulation time step versus particle size in the weak interaction regime (1) and strong interaction regime (2).

Regime	Diameter (nm)			
	<30	30	50	70
1	2.5 ns	400 ns	400 ns	400 ns
2	0.25 ns	10 ns	10 ns	10 ns

p-stripe, and the lateral extent corresponds to one period of our p–n array [6]. We neglect the movement in the Z-coordinate because the length of the p-stripe is orders of magnitude larger than the width of the charge depletion zone along the X-direction. Along the (vertical) Y-coordinate, we define the surface of the substrate as $Y = 0$, and set an upper boundary limit of 5 mm. For the theoretical analysis, we are interested in the effect of the particle size (d), electric field intensity (E), and the convective flow (v_{g}) on coverage selectivity. We explored the role of three parameters d, $-V_{\text{bias}}$, and U, in our simulations.

The boundary between regimes 1 and 2 is selected to be at $Y = 200$ nm; beyond this the electrostatic interaction between an incoming particle and the substrate is very small, $F_{\text{ext}} < 1$ pN. To maintain calculation accuracy, while reducing the required calculation time, we chose different simulation time steps, Δt, for regime 1 and 2, and for the different particle sizes. In regime 1, Δt was chosen as less than or equal to the time required for a particle to travel one mean free path. In regime 2, the particles are sufficiently close to the substrate that small effects of the choice of time step can lead to changes in the computed lateral location of deposition to the surface, so much smaller time steps were used in this region. Because the electrostatic force varies significantly with height and lateral location relative to the p–n junction, we chose time steps in regime 2 such that particles travel a distance no greater than the p-region of the depletion zone, Δw_{p} ($\sim$ 5 nm), in one time step, as calculated using the electrophoretic velocity, v_{e}. For a 30 nm sized particle, the required time to travel Δw_{p} is $\sim$10 ns for a field $E_{\text{s}} \sim 10^6$ V m^{-1}. The time steps are summarized in table 1.

The starting height of each particle trajectory was at $Y <= 10\ \mu$m, which turned out to be a maximum distance over which a particle would ever make it to the surface in the simulation volume considered. We began with randomly distributed particles over a region 15.5 μm in length along the X-direction, spanning a p–n junction. Our goal is to produce a one-dimensional simulation of the variation of the coverage across both p-type and n-type regions. To reduce the complexity and calculation time, we did not evaluate the forces in the Z-direction, i.e. parallel to the p-stripes. In the defined control volume with a periodic boundary condition in the X-direction, we considered particles convected by gas flow in two different directions along X: trajectory L is from the right to the left, and trajectory R is from the left to the right. Each trajectory calculation ends when the particle impacts the substrate.

In order to obtain reasonable statistics, we used a large number of trajectories, 50 000 for both the L and R cases. The final positions of the deposited particles were recorded as 1D simulated deposition patterns for trajectories of type L and R.

## 5. Comparison of simulation with experimental results

5.1. Effect of the electric field

Figure 3 shows SEM images of p–n junction-patterned substrates following particle deposition for both the smallest and largest diameter particles we investigated, under various reverse bias voltages. In our experiments, all Ag particles were negatively charged in the gas phase so that we see enhanced deposition in the n-type region under the influence of the electric field, as expected. Generally, the Ag nanoparticles were homogeneously distributed into both the n-type and p-type regions at low bias voltages, $(-V_{bias}) = 0.1$ V (figure 3(a)). With increasing reverse bias voltage, Ag particle deposition is enhanced in the n-type region over the p-type region (figures 3(b) and (c)). Significant particle-free zones are observed to either side of the p-type region (we discuss the asymmetry below) when $(-V_{bias}) = 0.9$ V (figure 3(d)). In our previous study [6], we observed analogous effects of the electric field on charged Ni nanoparticles. The raw images shown in figure 3 may give a misimpression about the effect of applied bias due to the fact that each deposition had a different extent of total particle deposit. Quantitatively processing the results presented in figure 3, we can determine the measured coverage selectivity for each particle size as a function of reverse bias voltage, and these are plotted as solid triangles in figure 4.

We next performed simulations, choosing similar parameters of reverse bias voltage, particle size, convective flow velocity, temperature and pressure to those used in the experiments. We see that, in qualitative agreement with experiment, the simulated coverage selectively (shown by the solid curves marked with squares) increases with increasing bias voltage for all three particle sizes, and that coverage selectivities very close to 100% are indeed predicted by the simulation at the highest bias voltages. In the simulation, this trend results from how the dominant forces act on the particles, mainly electrostatic, diffusion, and drag forces. However, our simulation predicts a coverage selectivity which initially increases with bias voltage at a rate ∼3 times faster than that observed experimentally.

The discrepancy between experiment and the simulations can be understood, at least qualitatively, if the potential drop across the surface of the p–n junction is reduced from that within the bulk. In fact, previous direct measurements of the surface potential across a Si p–n junction using scanning x-ray photoemission microscopy showed just such an effect [20]. Physically, at least part of this comes from the effect of electronically active surface states, which result in near-surface band bending. In principle the observed reduction might be used to calculate the density of surface states. In practice, however, the flux of ions to the surface drives the junction further from equilibrium, making such a calculation difficult. To account for this reduction we repeated the simulations, scaling the surface potential difference by an empirically determined factor of $\gamma = 0.3$. This produces good agreement between the simulation results (dashed lines marked by diamond points) and experimental data, as seen in figure 4, for all three particle diameters studied. Note that γ is an universal factor for various sized particles under different reverse bias conditions. This factor would be particle property independent, but may depend on the nature of the substrate.
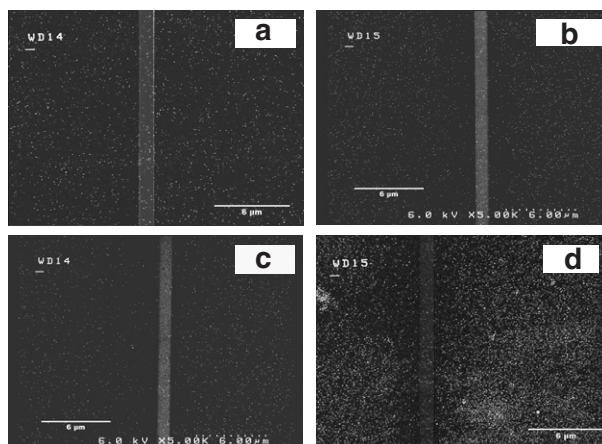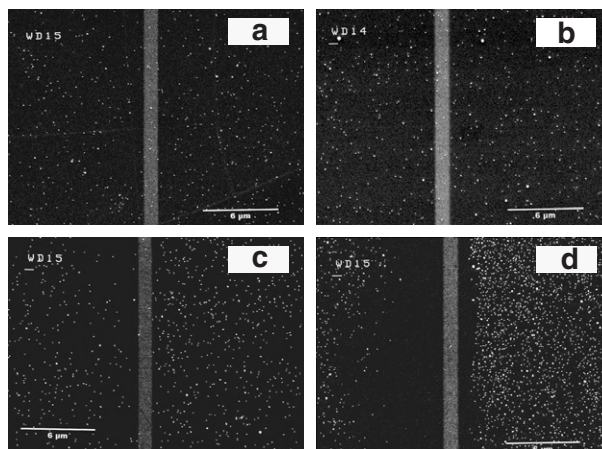

Figure 3. SEM images of Ag nanoparticle deposition patterns. Two different size particles, 30 and 70 nm, at four different applied bias conditions. (a) : −0.1 V; (b):−0.5 V; (c):−0.6 V; (d): −0.9 V. Scale bar: 6 μm.

5.2. The effect of the convective flow

The SEM images recorded at higher bias, where the selectivity is high, also show a clear asymmetry in the lateral extent of the particle-free zone. This asymmetry can be understood as due to the direction of convective flow; in figure 3(d) the flow is evidently from right to left. Figure 5 demonstrates this effect, for flows along this direction at a series of flow velocities. Figure 5(a) shows a simulated trajectory for a singly negatively charged 50 nm diameter particle across a p-type region in the absence of Brownian motion. The particle is initially attracted by the n-type depletion zone (position 1), but does not quite reach the substrate. Rather it continues above the p-type region, where the ionized acceptors electrically repel it, deflecting it upward as it moves out of that region (position 2). After leaving the p-type region, this particle is deflected downward by the attractive force from the ionized donors in the n-type depletion zone on the left side of the second junction (position 3). The heights of the 'lift-up' and 'drag-down' parts of the trajectory are determined by the flight time of a particle across the p–n junction and are inversely proportional to the convective flow velocity. As such the lift-up and drag-
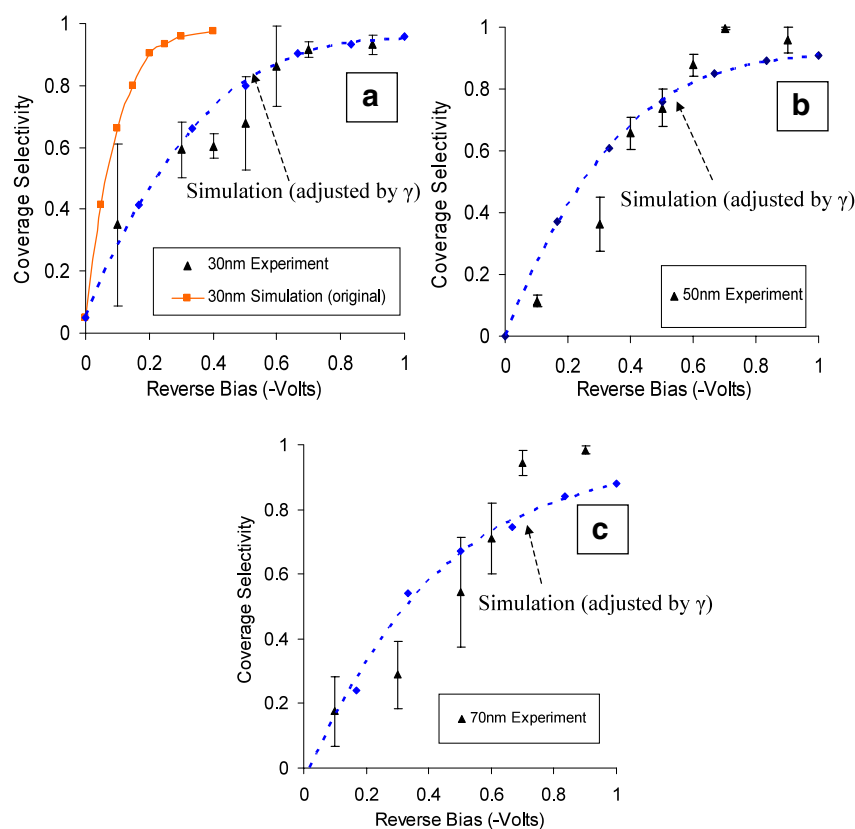
Figure 4. Coverage selectivity versus various reverse bias voltages. (a) 30 nm particles; (b) 50 nm particles; (c) 70 nm particles. Triangles: experimental data; squares: simulation data; diamonds: simulation data fitted by a factor, γ; dashed curve: fitted curve of the simulation data (diamonds).

down distance increases when the convective flow velocity is decreased. Simulations of single particle trajectories for increasing flow velocities are presented in figure 5(b). Without convective flow ($U = 0$), the particle travels nearly straight downward to the substrate with a slight lateral deflection due to the horizontal field component E_x. For the lower flow velocities illustrated, $U = 0.5, 1, 2$ m s^{-1}, the particle reaches the surface before entering the p–n junction; the lateral distance from the starting point to place of deposition is 1.5 μm, 2.4 μm and 3.6 μm respectively. On the other hand, particle 'lift-up' and 'drag-down' are observed for the larger two velocities, $U = 5, 10$ m s^{-1}. Decreasing U from 10 to 5 m s^{-1} causes the lift-up distance to increase from ∼0.2 to ∼0.5 μm, and the drag-down distance to increase from ∼0.03 to ∼0.04 μm, i.e. the lift-up height is approximately an order of magnitude larger than the drag-down distance, resulting in a net lift-up process when a particle crosses a p–n junction. Because the dopant concentration in the n-type region is lower than in the p-type region, the attractive force is weaker than the repulsive force [6]. As such, particles which cross the p–n junction are convected farther downstream before they are deposited. Due to the Y-directed electric field, and X-directed convective flow, it is difficult to avoid asymmetry in the deposition pattern. One possible way to reduce this would be to more closely approximate a stagnation point by having multiple particle inlet jets (micromachined) to minimize the X-component of the flow and have a flow that is more perpendicular to the substrate.

The convective flow, in addition to creating asymmetry in the deposit as discussed above, might be expected to affect coverage selectivity. To evaluate its effect we carried out simulations at variable gas velocity, v_g while F_{diff} and F_e were kept constant. Figure 6 presents the simulated coverage selectivity as a function of flow velocity for three different experimental conditions: 30 nm particles at $V_{bias} = -0.9$ V and -0.5 V respectively, and coverage selectivity for 70 nm particles at $V_{bias} = -0.5$ V. The results indicate that reducing the convective flow velocity only slightly enhances the coverage selectivity. Given this weak dependence, the convective flow velocity is neglected in the non-dimensional analysis to be presented later in the paper.

5.3. The effect of particle size

Figure 7 compares the measured and simulated coverage selectivity we obtained for three different applied reverse biases, as a function of particle diameters. The solid symbols show the experimentally determined values and the solid lines are the simulation results. While the simulation predicts that the coverage selectivity should decrease with increasing particle size, the experiment shows such a trend only for the smallest bias. At $V_{bias} = -0.3$ V (circular symbols) and $V_{bias} = -0.5$ V (triangular symbols), the experiment does show an inverse relationship between coverage selectivity and particle size. In contrast, the experiment clearly shows
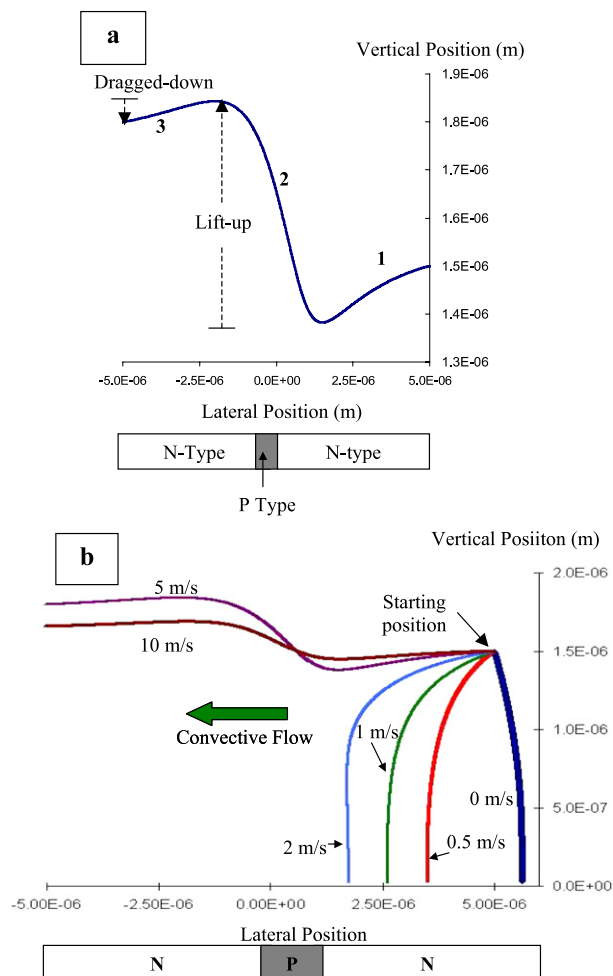
Figure 5. Analysis of a single particle trajectory without Brownian motion. (a) Trajectory of a particle at the p–n junction. Curve label 1: the particle was attracted by n-type depletion zone. Curve label 2: if not deposited, the particle is lifted up by the repulsive force from the p-type depletion zone. Curve label 3: when the particle was convected out of the p-type region, it was dragged down by the attractive force from the n-type depletion zone. (b) Particle trajectory at six different convective velocities, U : 0, 0.5, 1, 2, 5 and 10 m s^{-1}. Particle size: 50 nm. The applied bias voltage is -1 V.

Figure 6. Coverage selectivity versus the convective flow velocity obtained from simulation. U is the free-stream velocity used in the calculation (0.5–2 m s^{-1}).

Figure 7. Coverage selectivity versus particle size under three different reverse bias voltages: -0.3, -0.5, and -0.9 V. Negatively charged particles. Lines represent the simulation of coverage selectivity. The solid points are experimental coverage selectivity: square: $V_{bias} = -0.9$ V; triangle: $V_{bias} = -0.5$ V; sphere: $V_{bias} = -0.3$ V.

little size dependence or if anything a positive dependence on size, with selectivity of almost 100% for the 70 nm particle. The effect of particle size on coverage selectivity should reflect the size dependence of the competing forces acting on the particles. We note that the electrostatic force is directional and is independent of particle size. The diffusion force (equation (18)) has no preferred direction; due to the size effects on the no-slip boundary condition correction factor (C_c), the diffusion force over the range of particles being considered will have an approximately d^1 dependence. In our model these are the dominant forces, and thus the ratio F_e/F_{diff} should physically represent the extent of directional motion generated by the electrostatic force over non-directional Brownian motion, and should dominate the coverage selectivity. Thus in our simulations decreasing particle size increases the ratio F_e/F_{diff} (proportional d^{-1}) and therefore promotes higher coverage selectivity. This intuitive interpretation of the results clearly does not hold at higher
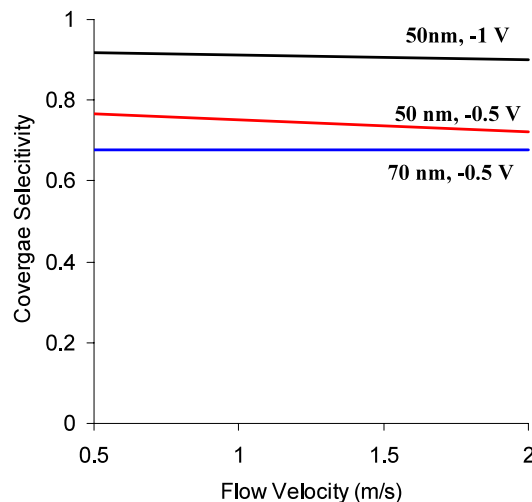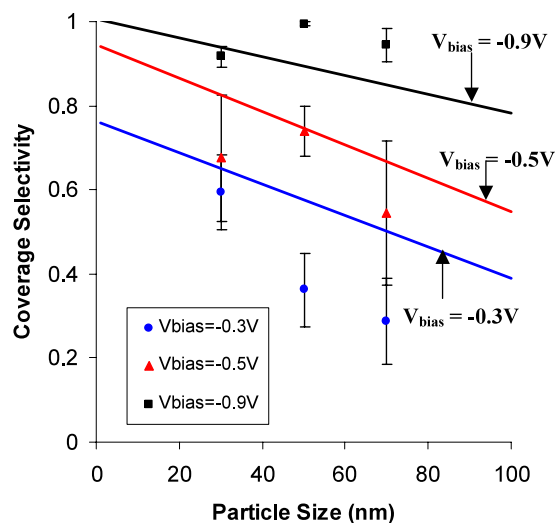
bias voltages, where the simulation predicts the same trends to hold as the lower bias cases although with higher selectivity. We defer the discussion of the discrepancy between simulation and experiment until we develop the non-dimension analysis in section 4.

5.4. Non-dimensional analysis

Because of the large number of variables that can affect the coverage selectivity, it is useful to employ a non-dimensional analysis. Clearly of central importance to coverage selectivity is the competition between the electrostatic force, which is the driving force for a patterned deposit, and the Brownian force, which tends to create a random deposit. Based upon our
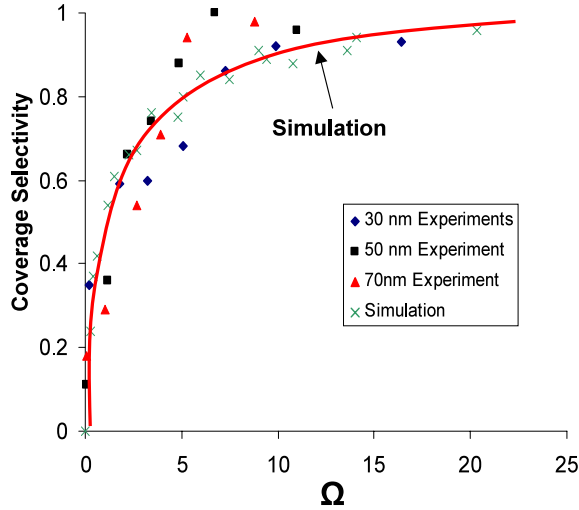
Figure 8. Non-dimensional analysis. Coverage selectivity versus Ω. Diamonds: experimental coverage selectivity of 30 nm particles; squares: experimental coverage selectivity of 50 nm particles; triangles: experimental coverage selectivity of 70 nm particles. The simulation curve, obtained from curve fitting of simulation data (crosses).

assignment of the dominant interactions, discussed in the last section, we now introduce a non-dimensional parameter, Ω, which is a ratio of kinetic energy generated by the electrostatic force, W_E, to the diffusion energy, W_{diff}.

$$\Omega = 100 \frac{w_e}{w_{\text{diff}}} = \frac{0.5 m_p v_e^2}{1.5 kT} = \frac{(ne E_y)^2}{3kT}$$
$$\times m_p B^2 \propto (V_{\text{bias}})^2 d^3 B^2 \propto V_{\text{bias}}^2 d^{-1} \qquad (19)$$

where v_e is the electrical drift velocity of a particle ($v_e = F_e^* B$), $B = \frac{C_C}{3\pi \mu d}$ is the mobility of a particle ($B \propto \sim d^{-2}$); the factor of 100 is just used for convenience. We evaluate E_y at a fixed position, $X = Y = 100$ nm, to have a simple relationship that E is linearly proportional to $(-V_{\text{bias}})$. The dependence of Ω on particle size and applied reverse bias given by equation (19) shows that $\Omega \propto d^{-1}$ and $\propto (-V_{\text{bias}})^2$.

We plotted our experimental data (triangle symbols) for coverage selectivity as a function of Ω, shown in figure 8. Also presented are the results of simulations, represented by the solid squares with a logarithmic curve fit (solid line). The clear correlation between coverage selectivity and Ω for the range of particle sizes, applied voltage, and conditions studied does indicate that this parameter provides a reasonable non-dimensional parameterization.

The modeling curve obtained by equation (19) agrees well with the experimental data particularly for $\Omega < 5$. Hence, one may conclude that the most important factors in this system are the electrostatic force and the diffusion force, which is affected primarily by the applied reverse bias voltage and particle size respectively. On the other hand, when $5 < \Omega < 10$, we see a clear deviation between the model and experimental results. This was observed earlier for 50 and 70 nm particles at high reverse bias conditions ($-V_{\text{bias}} > 0.7$ V, figure 7) where our model underpredicted the experimental coverage selectivity by about 10–15%. These discrepancies may arise from the additional effects that particles that deposit on the surface can

alter the effective field, through image forces, on subsequent particle deposition. We have observed experimentally that at higher deposition conditions the particles on a surface act as attractors to subsequent particle deposition relative to a bare surface.

We begin by evaluating the effect of particles previously deposited to the surface on subsequent deposition. It is well know from experiments on electrostatic particle precipitators that particles lose their charge when they deposit on a substrate (i.e. no Coulomb interaction with the gas-phase particles). As such, particle–particle interactions can be calculated from the combination of image and van der Waals forces $F_{\text{i\_pp}}$ and $F_{\text{vdw\_pp}}$ given by [12, 23]

$$F_{\text{i\_pp}} = -2 \left[\frac{d^2 (ne)^2}{8\pi \varepsilon_0 (S+d)^3} - \frac{2d^2 (S+d)(ne)^2}{\pi \varepsilon_0 [4(S+d)^2 - d^2]^2} \right] \quad (20)$$

$$F_{\text{vdw\_pp}} = -\frac{32 A_H}{3} \frac{(\frac{d}{2})^6}{S^2 (S+2d)^2 (S+d)^3}. \quad (21)$$

Here, A_H is the Hamaker constant (4×10^{-19} J), and S is the particle–particle distance. F_{i_pp} is negligible ($\sim < 10^{-10}$ pN when $S = 90$ nm) compared to F_e (~ 0.003 pN when $S = 90$ nm, $X = 2L_p$, and $V_{\text{bias}} = -0.7$ V). Considering F_{vdw_pp}, equation (21) indicates that larger sized particles will increase the attractive force to incoming particles. For example, when S is 90 nm, $F_{\text{vdw\_}pp}$ is 1.5×10^{-4} pN for a 30 nm particle, but increases by a factor of 20 to 3×10^{-3} pN for a 70 nm particle, which is about equivalent to F_e (~ 0.003 pN). At high coverage selectivity and high surface coverage, the deposited particles in the n-type region can assist the incoming particles to be deposited to enhance this coverage selectivity. This effect should most affect the larger particles. In our studies the discrepancy between experiment and model occurs at intermediate values of Ω. While we are not in a position to firmly establish this point we believe this is likely because at low values of coverage selectivity (i.e. low Ω) the low substrate coverage mitigates the effects of particle–particle forces, while at high values of Ω the coverage selectivity is already so high as to mask these effects. Thus we only see these effects at the intermediate values of Ω where high coverage density effects of particle–particle interaction can impact the overall coverage selectivity. A more thorough analysis would require a detailed analysis and correlation of particle deposition versus particle–particle separation distance for various particle sizes, and is beyond the scope of this work. Generally, the minimum coverage selectivity can still be estimated by Ω without taking into account the particle–particle interaction.

We have previously demonstrated that we can obtain selective deposition with positively charged particles [6]. By changing the particle polarity, the n-type region now becomes repulsive. Equation (19) is still applicable for this case; however, to make the geometric adjustment (the width of attractive zone is 1 μm and the width of repulsive zone is 30 μm), we introduce a new dimensionless parameter, Ω_2 ($= K_2 \Omega$, K_2 is a geometry adjusting factor) to evaluate the performance for depositing particles on the p-type region. For polydisperse particles (the peak mobility diameter is 50 nm), K_2 is found to be ~ 0.4 by fitting the coverage selectivity results [6]. The implication is that one must increase the reverse bias voltage in order to obtain the same Ω.

This analysis indicates that Ω is an effective indicator of process performance. If one desires greater than 80% coverage selectivity, then Ω should be least 6. However, the use of the present form of Ω implies that inertial effects are relatively weak in comparison with electrostatics, drag, and diffusion forces. As such this non-dimensional analysis is limited to higher pressure situations where ballistic deposition is unimportant.

6. Conclusion

The electrostatic-directed assembly approach has been demonstrated as an effective method for positioning nanoparticles. A Brownian dynamic simulation has been developed that can semi-quantitatively explain most of the behavior observed experimentally, and can be extended to other geometric and process conditions. A non-dimensional parameter Ω is developed which provides a guide to expected coverage selectivity.

References

[1] Su K H, Wei Q H, Zhang X, Mock J J, Smith D R and Schultz S 2001 *Nano Lett.* **3** 1087
[2] Kruis F E, Fissan H and Peled A 1998 *J. Aerosol Sci.* **29** 511–35
[3] Barry C R, Steward M G, Lewin N Z and Jacobs H O 2003 *Nanotechnology* **14** 1057–63
[4] Jacobs H O, Campbell S A and Steward M G 2002 *Adv. Mater.* **14** 1553
[5] Krinke T J, Deppert K, Magnusson M H and Fissan H 2002 *Part. Part. Syst. Charact.* **19** 321–6
[6] Tsai D H, Kim S H, Corrigan T D, Phaneuf R J and Zachariah M R 2005 *Nanotechnology* **16** 1856–62
[7] Pluym T C, Powell Q H, Gurav A S, Ward T L, Kodas T T, Wang L M and Glicksman H D 1993 *J. Aerosol Sci.* **23** 383
[8] Corrigan T D, Guo S, Phaneuf R J and Szmacinski H 2005 *J. Fluoresc.* **15** 777–84
[9] Fissan H, Helsper C and Thielen H J 1983 *J. Aerosol Sci.* **14** 354–7
[10] Chen D and Pui D Y H 1999 *J. Nanopart. Res.* **1** 115
[11] Schlichting H 1979 *Boundary-Layer Theory* 7th edn (New York: McGraw-Hill)
[12] Krinke T J, Deppert K, Magnusson M H, Schmidt F and Fissan H 2002 *J. Aerosol Sci.* **33** 1341–59
[13] Fuchs N A 1963 *Geophys. Pura Appl.* **56** 185
[14] Wiedensohler A 1988 *J. Aerosol Sci.* **10** 387
[15] Kan H C and Phaneuf R J 2001 *J. Vac. Sci. Technol.* B **19** 1158
[16] Ermak D L and Buckholz H 1980 *J. Comput. Phys.* **35** 169–82
[17] Park H, Kim S and Chang H S 2001 *J. Aerosol. Sci.* **32** 1369–88
[18] Hinds W C 1998 *Aerosol Technology* 2nd edn (New York: Wiley–Interscience)
[19] Kadaksham A T J, Singh P and Aubry N 2004 *Electrophoresis* **25** 3625
[20] Phaneuf R J, Kan H C, Gregoratti L, Gunther S and Kiskinova M 2000 *J. Appl. Phys.* **88** 863–8
[21] Mahadevan R, Lee D, Sakurai H and Zachariah M R 2002 *J. Phys. Chem.* A **106** 11083
[22] Kim S H and Zachariah M R 2005 *Nanotechnology* **16** 2149
[23] Grobelny J, Tsai D H, Kim D I, Pradeep N and Zachariah M R 2006 *Nanotechnology* **17** 5519